Advanced Functional Materials

ADVANCED FUNCTIONAL MATERIALS
www.afm-journal.de

RESEARCH ARTICLE OPEN ACCESS

Speckle-Engineered Upconversion Amplification in Nanoemulsion-Templated Hydrogel Microdomes

Chaeyeong Ryu[1] | Byungcheon Yoo[1] | Seunghun Lee[2] | Hyungyo Jeong[1] | Sanggyun Jeong[1] | Heesu Cho[1] | Jongwon Oh[1] | Dahye Baek[1] | Jongkyu Kim[1] | Yubin Lee[1] | Eunsu Gu[1] | Dong-Hwan Kim[3] | Jung-Hoon Park[2] | Jiseok Lee[1]

[1]School of Energy and Chemical Engineering, Ulsan National Institute of Science and Technology (UNIST), Ulsan, Republic of Korea | [2]Department of Biomedical Engineering, Ulsan National Institute of Science and Technology (UNIST), Ulsan Metropolitan City, Republic of Korea | [3]School of Chemical Engineering, Sungkyunkwan University (SKKU), Suwon, Republic of Korea

Correspondence: Dong-Hwan Kim (dhkim1@skku.edu) | Jung-Hoon Park (jh.park@unist.ac.kr) | Jiseok Lee (jiseok@unist.ac.kr)

Received: 14 December 2025 | **Revised:** 28 March 2026 | **Accepted:** 15 April 2026

Keywords: hydrogel | maskless lithography | nanoemulsion | soft photonics | upconversion nanocrystals

ABSTRACT

Hydrogel-based photonic systems integrating luminescent emitters offer promise as soft, reconfigurable optical platforms, yet most designs lack internal optical engineering to control light propagation and confinement. Here, we present a lithographically programmable soft-photonic platform in which upconversion nanocrystals (UCNs) encapsulated within fluorocarbon nanoemulsion droplets are embedded in a poly(ethylene glycol) diacrylate (PEGDA) hydrogel microdome. Upon drying, strong refractive index contrast between the PEGDA matrix and fluorocarbon droplets creates a cooperative optical microenvironment that structures the near-infrared (NIR) excitation beam into a speckle-like field with localized hot spots while extending the photon dwell time within the microdome via internal reflection-based waveguiding. These effects yield a fully reversible, greater than sevenfold enhancement of upconversion luminescence—well beyond simple concentration or mechanical densification. This optical gain originates from multiple-scattering-assisted speckle excitation activated only in the contracted microdome state. Because UCNs are pumped by invisible NIR speckle illumination that rapidly varies in 3D across the microdome height, the incoherent sum of the photoluminescence manifests as a homogeneous filter-free visible brightness increase. The hydrogel microdomes, fabricated via a customized digital micromirror device (DMD)-based microlithography, enable high-resolution patterning of moisture-responsive displays, multicolor emission motifs, and reversible QR-code encryption, establishing a scalable route toward speckle-engineered soft photonic systems.

1 | Introduction

Hydrogel-based photonic systems have attracted considerable attention as deformable optical platforms that respond to environmental stimuli, including temperature [1, 2], humidity [3–5], pH [6, 7], and chemical stimuli [8–10]. By coupling mechanical softness with optical responsiveness, these systems offer distinct advantages for biosensing [11, 12], tunable optics [13], soft robotics [14, 15], and dynamic displays [16–18]. In particular, integrating luminescent species—such as organic dyes [19, 20], quantum dots [21, 22], or lanthanide-doped nanocrystals [23, 24]—into hydrogel matrices enables stimuli-responsive emitters whose intensity, color, and spatial profile can be modulated by swelling or other external inputs. Among these emitters, lanthanide-doped

Chaeyeong Ryu and Byungcheon Yoo contributed equally to this work.

upconversion nanocrystals (UCNs) are especially attractive owing to their ability to absorb low-energy near-infrared (NIR) photons and emit higher-energy visible light via anti-Stokes processes [25]. Their deep penetration, low background autofluorescence, and excellent photostability make them promising for biomedical imaging, volumetric displays, and anti-counterfeiting [26–31]. However, their inherently low quantum yield—typically below 1 % under practical excitation conditions—has constrained their application in high-performance photonic devices [32, 33]. Efforts to enhance UCNs emission have typically followed two main routes: intrinsic chemical strategies and extrinsic optical environment engineering. Intrinsic approaches involve tailoring nanoparticle composition to suppress non-radiative loss and improve energy transfer through core–shell architecture [34], dopant concentration optimization [35], lattice selection [36], or surface ligand modification [37]. While effective at the materials level, these strategies often require complex synthesis and offer limited scalability. Extrinsic approaches instead engineer the optical surroundings by integrating UCNs with photonic crystals [38, 39], plasmonic structures [40, 41], dielectric resonators [42], or waveguides [43], thereby amplifying excitation and emission through local-field enhancement and photonic manipulation. Yet such architecture typically relies on rigid substrates and lithographically defined nanostructures, making them poorly compatible with soft, deformable, and scalable platforms.

Hydrogels provide a 3D, aqueous-compatible, and mechanically tunable network that can serve as a soft and adaptive photonic medium [44, 45]. Unlike rigid photonic architectures, they can undergo large, reversible volume changes, offering a route to dynamically reconfigurable light–matter interactions [46]. Most luminescent hydrogels, however, rely primarily on changes in emitter density during swelling and deswelling, yielding only modest intensity modulation and affording limited control over light propagation or confinement [47, 48]. Without internal optical engineering—such as refractive index contrast or embedded scattering domains—light–matter interactions remain inefficient. An alternative strategy is to optically engineer the hydrogel host by introducing high–refractive index–contrast nanodomains that, upon drying, generate a disordered scattering landscape. In such media, multiple scattering extends the effective photon path length and can create speckle-like excitation hot spots, thereby enhancing the probability of absorption and emission events. For lanthanide-doped UCNs—whose emission arises from nonlinear, multiphoton absorption—this structurally defined excitation field is particularly effective. Moreover, because UCNs are pumped by near-infrared light that is invisible to the human eye, the structurally induced enhancement manifests as a clean, filter-free increase in visible luminescence—unlike downconversion dye systems excited in the visible range, where structural amplification inevitably brightens both excitation leakage and emission, degrading naked-eye contrast without optical filters. Embedding such scattering nanodomains within hydrogels thus offers a promising route to soft optical amplifiers that couple volumetric deformation with high-contrast, filter-free luminescence control.

In this study, we introduce a structurally reconfigurable and digitally patternable soft photonic platform based on nanoemulsion-confined hydrogel microdomes for the dynamic modulation and amplification of upconversion luminescence, extending speckle-based light management—previously limited to rigid systems—into soft, stimuli-responsive materials. Size-controlled, UCN-loaded FC-40 nanoemulsion droplets are embedded in a poly(ethylene glycol) diacrylate (PEGDA) hydrogel matrix, creating an internal optical landscape that exploits strong refractive index contrast and spatial confinement to activate cooperative light-amplification effects. In the dry, contracted state, multiple scattering and interference at the nanoemulsion–hydrogel generate a speckle-like excitation field with localized high-intensity hot spots, effectively increasing the local excitation fluence experienced by the nonlinear UCNs. Simultaneously, total internal reflection within the hydrogel microdomes increases photon path length, or in other words, the photon dwell time of the excitation beam within each microdome, thereby further amplifying light-UCN interactions for photoluminescence generation. Acting together, these effects produce a reversible, nonlinear luminescence enhancement exceeding sevenfold—well beyond what is achievable through emitter concentration or simple densification alone. The microdome structures are fabricated using a customized digital micromirror device (DMD)-based maskless lithography system, enabling scalable, high-resolution patterning with arbitrary geometry. Through systematic control experiments, we decouple physical densification from optical confinement and confirm that the observed enhancement is driven by structural light management. Finally, we demonstrate programmable photonic functionalities—including moisture-triggered message reveal and reversible QR-code encryption—that highlight the platform's potential for optical security and smart labeling.

2 | Results

2.1 | Hydrogel Microdome Design for Reversible Modulation and Amplification of Upconversion Luminescence via Optical Confinement Effects

To achieve reversible modulation and amplification of upconversion luminescence via structural light confinement, we designed a hydrogel microdome photonic system in which UCN-loaded nanoemulsion droplets are confined within a crosslinked PEGDA matrix. The volumetric responsiveness of microdomes enables structural and optical reconfiguration upon hydration, providing dynamic control over speckle-assisted luminescence enhancement. Lanthanide-doped hexagonal-phase UCNs were first synthesized and dispersed in fluorocarbon oil (FC-40) to form the oil phase. This oil phase was emulsified into an aqueous solution (continuous phase) containing PEGDA700, photoinitiator (Darocur 1173), and nonionic surfactant Pluronic F-68 (PF-68) (Figure 1a). High-pressure homogenization produced a uniform, stable oil-in-water nanoemulsion in which UCNs were encapsulated within FC-40 droplets, allowing control over droplet size and homogeneous distribution of UCNs (Figure 1b). Subsequent 365 nm UV exposure induced photopolymerization of the PEGDA phase, yielding a covalently crosslinked hydrogel network in which the UCN-loaded FC-40 nanoemulsion droplets are stably immobilized (Figure 1c). To generate spatially defined microstructures, this photocurable nanoemulsion ink was patterned using a customized DMD-based maskless lithography setup [36, 49–51]. Programmable circular masks produced arrays of microdomes with controlled lateral dimensions, height, and spacing (Figure 1d, **top**). Centimeter-scale arrays of microdomes

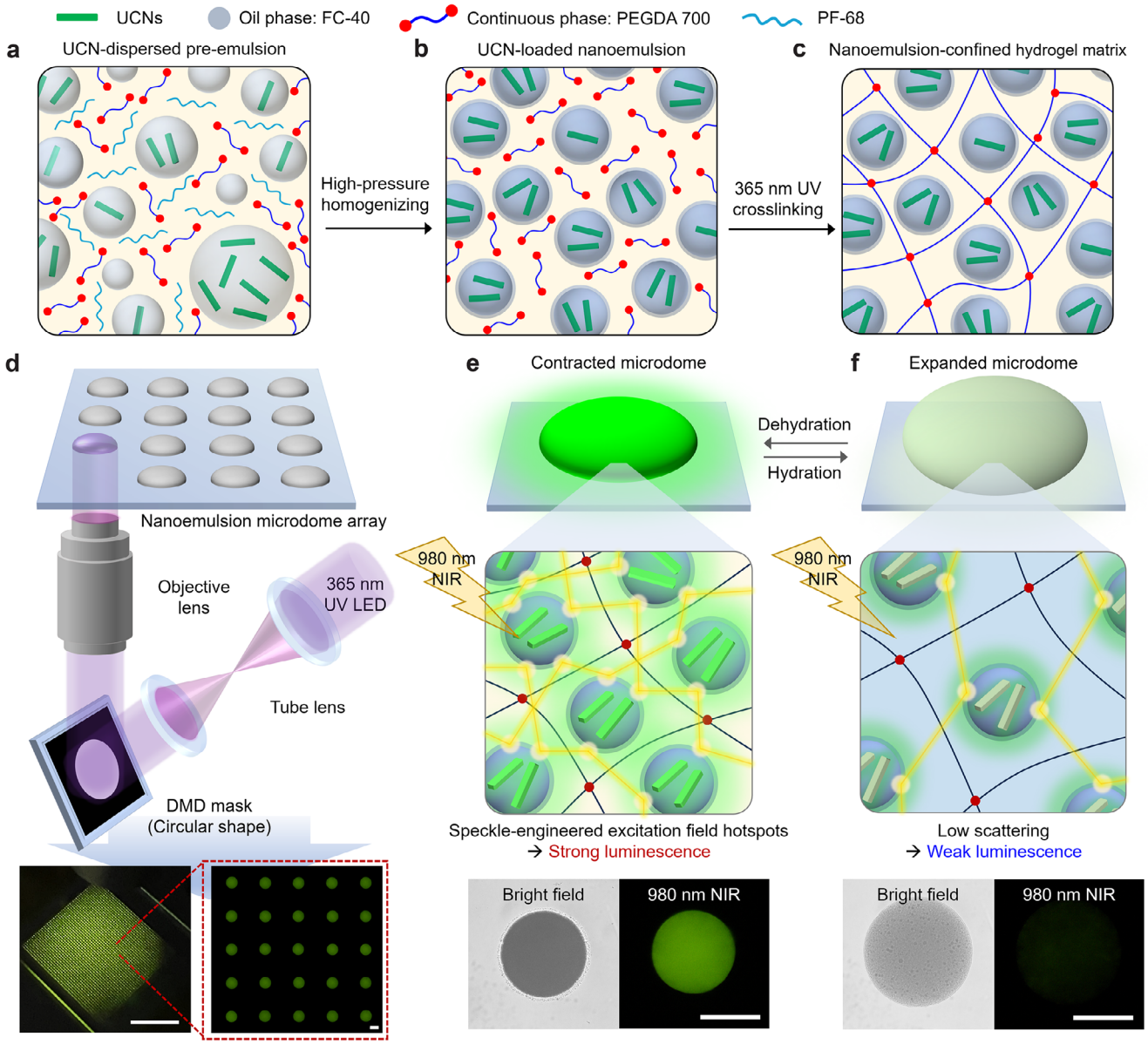

FIGURE 1 | Fabrication of structurally reconfigurable microdome arrays for speckle-engineered upconversion luminescence enhancement. (a) Pre-emulsion formed by dispersing UCN-loaded FC-40 oil droplets into an aqueous PEGDA/PF-68 solution. (b) High-pressure homogenization generates uniform UCN-loaded FC-40 nanoemulsion droplets. (c) UV photo-crosslinking encapsulates UCN-loaded nanoemulsion droplets within a hydrogel network. (d) DMD-based microlithography patterns microdomes (top), and a centimeter-scale microdome array displaying homogeneous green luminescence (bottom). (e,f) Schematic and corresponding bright-field/luminescence images of contracted (dry) and expanded (swollen) states showing reversible luminescence switching. Scale bars: (d, left) 1cm; (d, right) 100 μm; (e and f) 100 μm.

fabricated via DMD lithography display homogeneous green upconversion luminescence across the entire field of view. Magnified regions confirm consistent emission from individual domes. (Figure 1d, **bottom**).

These microdomes exhibit hydration-dependent structural and optical changes. In the dehydrated (contracted) state, the PEGDA network retains densely packed UCN-loaded nanoemulsion droplets, maximizing the refractive index contrast among PEGDA ($n \approx 1.46$), FC-40 ($n \approx 1.29$), and the surrounding air ($n = 1.00$). This configuration generates a multiply scattering, speckle-like NIR excitation field with localized hot spots, while simultaneously increasing photon dwell time via internal reflection within the dome geometry, resulting in bright upconversion luminescence (Figure 1e). Upon water uptake, the hydrogel swells and the inter-droplet spacing increases within a hydrated PEGDA–water matrix of lower effective refractive index ($n \approx 1.38$). This index matching weakens speckle formation and substantially increases the total internal reflection angle, resulting in diminished luminescence (Figure 1f). The bottom panels of Figure 1e and f visualize this reversible transition: bright-field images show that hydrated microdomes become more transparent due to reduced scattering upon swelling, while 980 nm–excited luminescence images reveal a pronounced decrease in green upconversion brightness. Beyond this intensity modulation, the emission remains spatially uniform across each dome in both states,

indicating that the nanoemulsion droplets and the underlying optical microenvironment are preserved throughout repeated hydration–dehydration cycles. These results demonstrate that nanoemulsion-confined PEGDA microdomes provide a robust, digitally patternable architecture for implementing speckle-based optical confinement and reversible amplification of upconversion luminescence.

2.2 | Encapsulation of UCNs in Nanoemulsion Droplets

Nanoemulsions are kinetically stable oil-in-water dispersions characterized by submicron droplet sizes, typically below a few hundred nanometers [52, 53]. In this study, we employ a fluorocarbon-based nanoemulsion to embed discrete, low-refractive index domains within a PEGDA hydrogel matrix, thereby establishing the internal refractive index contrast for light confinement and amplification. The precursor solution consists of two immiscible phases: an aqueous phase containing 36 % (v/v) PEGDA, 59 % (v/v) water, and 5 % (v/v) of the nonionic surfactant PF-68 (100 mL total), and an oil phase comprising FC-40 loaded with 1 g of lanthanide-doped UCNs (50 mL) (Figure 2a-i; Figure S1). Mechanical stirring of the biphasic mixture produces a coarse pre-emulsion in which irregularly sized, UCN-loaded FC-40 droplets are dispersed in the aqueous PEGDA/PF-68 solution (Figure 2a-ii). This pre-emulsion is then subjected to high-pressure homogenization at 15 000 psi for up to 10 passes, yielding a well-defined oil-in-water nanoemulsion with narrowly distributed droplet sizes (Figure 2a-iii). Transmission electron microscopy (TEM) confirms the encapsulation and spatial confinement of UCNs (Figure 2b). The β-phase $NaYF_4$:Yb^{3+}/Er^{3+}/Gd^{3+} UCNs, synthesized via a conventional hydrothermal route, appear as rod-like nanocrystals (**left panel**). After high-pressure homogenization, individual rods are clearly observed within FC-40 droplets (**middle panel**), and these droplets remain embedded and immobilized within the photo-crosslinked PEGDA hydrogel network (**right panel**). The corresponding photoluminescence spectrum shows a green upconversion peak near 550 nm under 980 nm excitation, consistent with the stoichiometrically optimized dopant composition (Figure 2c).

To qualitatively assess nanoemulsion uniformity, we compared the emission from pre-emulsion and nanoemulsion samples at multiple positions. In the pre-emulsion state, large and polydisperse oil droplets—together with sedimented UCN aggregates outside droplets—lead to pronounced spatial fluctuations in emission intensity. In contrast, samples that underwent more than 10 homogenization passes display visually homogeneous luminescence (Figure 2d) and no visible phase separation between oil and aqueous phases, with line scans revealing nearly constant intensity across the field of view (Figure 2e).

To quantify these observations, dynamic light scattering (DLS) was further used to quantify droplet size as a function of homogenization passes. After 5 passes, the emulsion exhibits a relatively broad size distribution with a polydispersity index (PDI) of approximately 0.1. Beyond 10 passes, the PDI drops below 0.047, indicating a highly monodisperse nanoemulsion with an average droplet diameter of 340 nm (Figure 2f; Table S1). Zeta potential measurement yields a value of approximately −22 mV, reflecting sufficient electrostatic and steric stabilization provided by PF-68 to suppress droplet coalescence and maintain colloidal stability over time (Figure 2g). Taken together, these results confirm that hydrophobic UCNs can be dispersed within FC-40 nanoemulsion droplets with high uniformity (PDI< 0.05) and colloidal stability ($\zeta \approx -22$ mV), obviating the need for additional surface treatments such as silica coating or fluorinated ligand functionalization.

2.3 | Structural Optical Confinement Drives Enhancement of Upconversion Emission

A single microdome was prepared by exposing the UCN-loaded nanoemulsion precursor solution containing the photoinitiator to patterned 365 nm illumination using a customized DMD-based maskless microlithography system onto an acrylated glass substrate. The resulting PEGDA hydrogel effectively encapsulates the UCN-loaded nanoemulsion droplets within a crosslinked PEGDA matrix whose volume can reversibly expand upon hydration and contract upon dehydration (Movie S1). These intrinsic features of the hydrogel network give rise to pronounced reversible changes in UCN luminescence under 980 nm excitation (Movie S2). In the swollen state, the emission is strongly attenuated and can be regarded as effectively "off"; upon dehydration, the luminescence turns "on" with markedly enhanced brightness (Figure 3a). The photoluminescence spectra confirm that the characteristic Er^{3+} bands (~540 and 655 nm) intensify dramatically by approximately sevenfold in the contracted state and nearly vanish upon rehydration, demonstrating robust reversibility over repeated cycles (Figure 3b). Peak-normalized spectra further show that the hydrated and dehydrated spectra overlap closely after normalization to the Er^{3+} green-band maximum, indicating that hydration predominantly scales the emission intensity without appreciable changes in spectral shape or the red-to-green ratio (Figure S2 and Table S2). Consistent with this intensity-only scaling, the green-dominant appearance in camera images should not be interpreted as selective detection of the green band; instead, it reflects the wavelength-dependent responsivity of silicon-based RGB sensors (reduced sensitivity in the far-red) together with built-in NIR-rejection optics commonly present in commercial cameras. Accordingly, all photographs shown in the manuscript correspond to the camera's full merged RGB output under 980 nm excitation (Figure S3). Moreover, photoluminescence lifetime measurements show no measurable change between the hydrated and dehydrated states (Note S2 and Figure S4), confirming that the intrinsic emission efficiency of the UCNs remains unchanged. These results collectively demonstrate that the observed switching and amplification originate from hydration-controlled optical light management in the microdome architecture, rather than from any modification of the intrinsic emitter properties.

Upon dehydration, water evaporation causes the microdome to contract, increasing the local density of encapsulated nanoemulsion droplets. More importantly, this contraction, combined with the presence of FC-40 droplets, generates a porous microstructure with high refractive index contrast among the PEGDA matrix ($n \approx 1.46$), FC-40 droplets ($n \approx 1.29$), and the surrounding air ($n = 1.00$). Cross-sectional SEM images of freeze-dried microdomes directly visualize this structural transformation (Figure 3c; Figure S5).

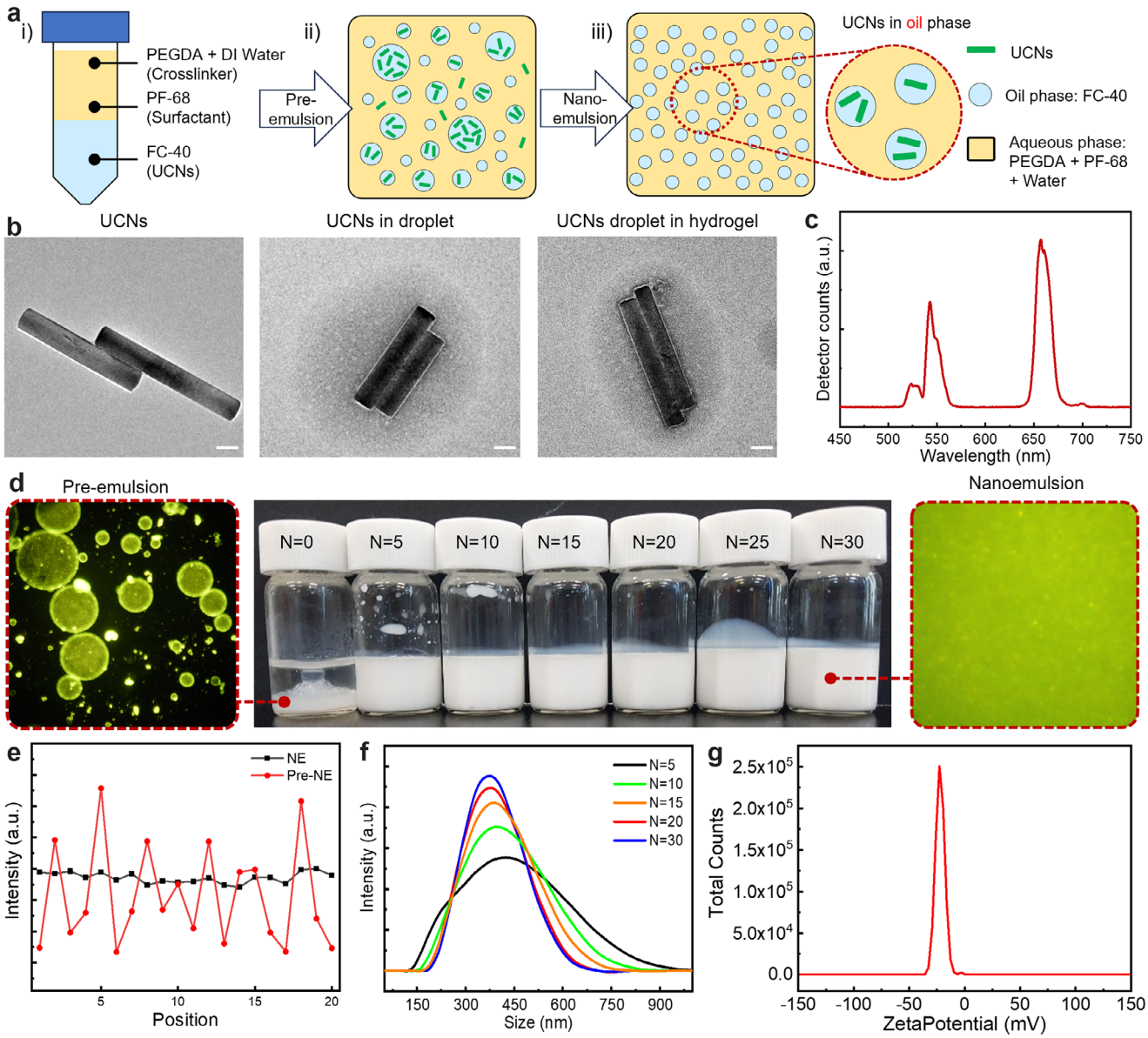

FIGURE 2 | Preparation and characterization of UCN-loaded nanoemulsion droplets. (a) Schematic of the nanoemulsion formulation process: (i) UCNs dispersed in FC-40 combined with aqueous PEGDA/DI water/PF-68 solution; (ii) mechanical stirring produces a coarse pre-emulsion; (iii) high-pressure homogenization yields a uniform oil-in-water nanoemulsion. (b) TEM images of UCNs (left), UCNs within FC-40 droplets (middle), and UCN-loaded nanoemulsion droplets embedded in PEGDA hydrogel (right). Scale bars: 50 nm. (c) Upconversion emission spectrum of the nanoemulsion under 980 nm excitation. Spectra are shown as raw spectrometer counts (a.u., not normalized) acquired under identical conditions (500 mW; 220 μm spot size). Spectral acquisition conditions are detailed in Note S1 (d) Luminescence comparison of pre-emulsion and nanoemulsion (N = 0–30 passes). (e) Spatial intensity profiles of luminescence from pre-emulsion and nanoemulsion. (f) DLS-measured droplet size distributions as a function of homogenization passes. (g) Zeta potential measurement confirming colloidal stability of the nanoemulsion.

To preserve the internal morphology, samples in both hydrated and dehydrated states were rapidly frozen in liquid nitrogen and subsequently lyophilized. In the dehydrated state, the PEGDA matrix is already contracted around the FC-40 droplets prior to freezing; upon lyophilization, the low-boiling-point FC-40 evaporates, leaving well-defined spherical pores that reflect the original droplet size and distribution. The uniform pore size is consistent with the monodisperse droplet distribution achieved by high-pressure homogenization. In contrast, the hydrated microdome is frozen while the PEGDA network remains swollen with water; during lyophilization, ice sublimation causes the expanded polymer network to collapse, filling the space around the nanoemulsion droplets and resulting in a relatively smooth, continuous morphology with no discernible pore structure.

To disentangle simple volumetric effects from optical confinement mechanisms, we employed a controlled volumetric tuning strategy using PEG200–water mixtures of varying composition (Figure 3d). PEG200 permeates the porous network without significantly swelling the polymer chains, enabling osmotic adjustment of the microdome volume while keeping the internal pores filled with liquid rather than air. As the external PEG200 fraction

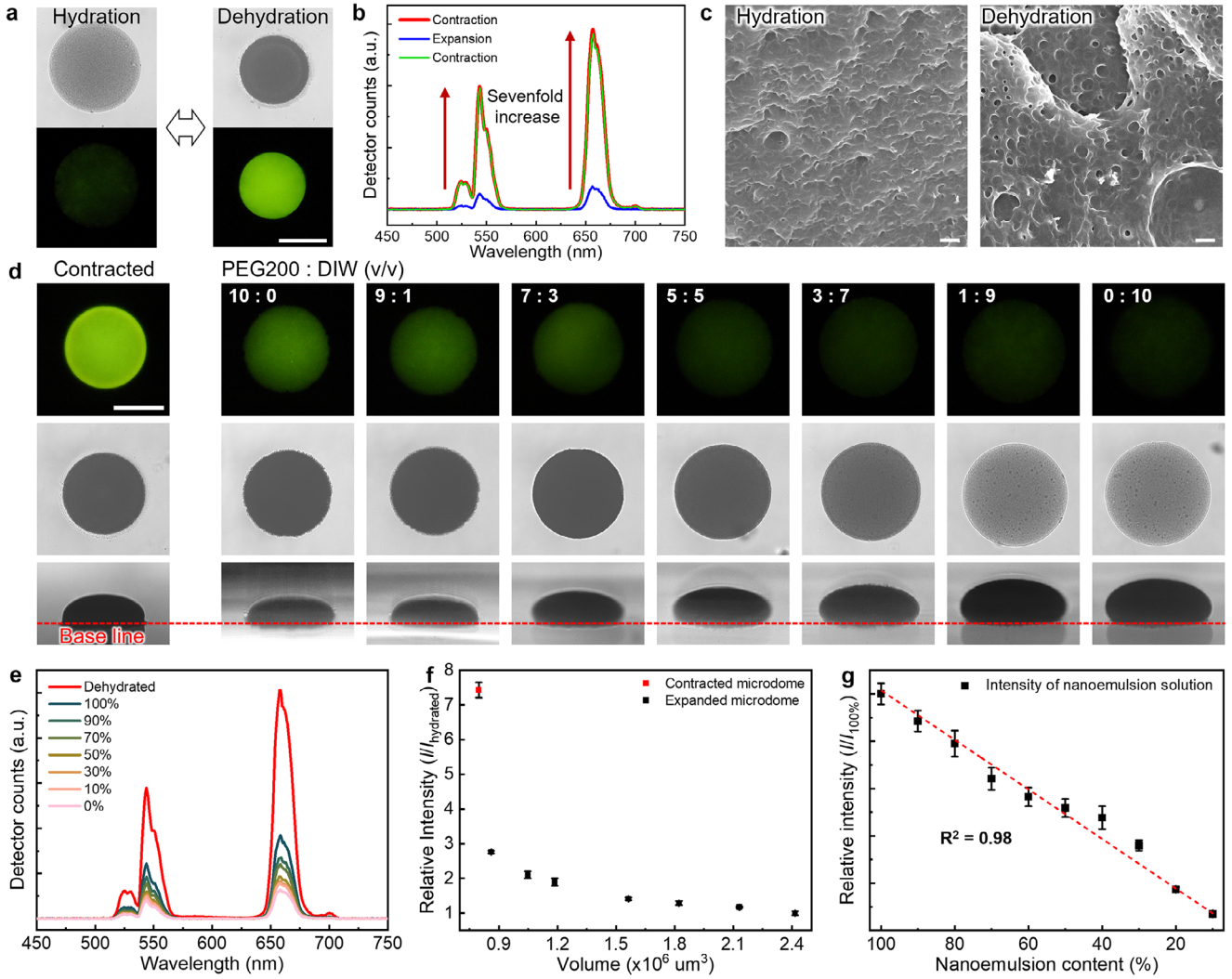

FIGURE 3 | Upconversion luminescence amplification in dried UCN-loaded nanoemulsion microdomes beyond simple volumetric effects. (a) Bright-field and luminescence images of a single microdome in the expanded and contracted states. Scale bar: 100 μm. (b) Upconversion emission spectra confirming sevenfold luminescence intensity increase. (c) Cross-sectional SEM images of freeze-dried microdomes in hydrated and dehydrated states. Scale bar: 1 μm. (d) Bright-field and luminescence images of microdomes equilibrated in PEG200/DIW mixtures at varying volume ratios. Scale bar: 100 μm. (e) Corresponding photoluminescence spectra as a function of PEG200 content. (f) Relative upconversion intensity as a function of microdome volume. Integrated emission is plotted as relative intensity (I/I_{hydrated}), where I_{hydrated} is the integrated emission of the fully expanded microdome in DI water. (g) Upconversion intensity of diluted nanoemulsion solutions plotted as relative intensity ($I/I_{100\,\%}$), where $I_{100\,\%}$ is the undiluted sample.

increased, the microdome volume decreased progressively, resulting in a modest ~2.5-fold increase in emission intensity accompanied by reduced optical transmittance (Figure 3d,e; Figure S6). Consistent with this interpretation, normalized spectra across the PEG200 series (Figure S7) exhibit similar band shapes, and the corresponding red-to-green peak ratio remains nearly constant, suggesting that PEG200-driven volume tuning mainly modulates overall brightness rather than altering the intrinsic UCN emission pathways. Notably, when the surrounding medium consisted of pure PEG200, the microdome volume approached that of the fully dehydrated state; however, air-dried microdomes still exhibited approximately 2.5-fold higher emission intensity than their PEG200-immersed counterparts at comparable volumes (Figure 3f). Here, the intensity is reported as relative intensity (I/I_{hydrated}), where I_{hydrated} is the integrated emission measured from the fully expanded microdome in DI water under identical acquisition settings. This intensity offset at matched volumes indicates that dehydration introduces an additional optical gain beyond volumetric densification alone. This difference can be attributed to the distinct refractive index landscapes in the two states: in the dried microdome, high contrast among PEGDA ($n \approx 1.46$), FC-40 ($n \approx 1.29$), and air ($n = 1.00$) maximizes both multiple scattering and waveguiding effects, whereas in the PEG200-filled microdome, the similar refractive indices of PEGDA and PEG200 ($n \approx 1.45$) diminish these optical effects. The critical role of refractive index contrast was further verified by comparing nanoemulsion systems with different oils (Figure S8). In the case of silicone oil nanoemulsion ($n \approx 1.4$), the solution appeared nearly transparent due to the small refractive index difference with PEGDA. Although this system showed approximately 5-fold enhancement when dried, this increase started from a significantly weaker baseline intensity; consequently, the absolute emission intensity remained substantially lower than that of the FC-40 system, which achieved greater than 7-fold enhancement.

Moreover, PEGDA solution containing bare hydrophilic UCNs without oil droplet emulsion completely eliminated the scattering interface and showed minimal emission, confirming that the nanoemulsion-induced refractive index heterogeneity is essential for luminescence amplification.

To further confirm that the enhancement does not arise from simple emitter densification, we examined the luminescence intensity of UCN-loaded nanoemulsion solutions in the absence of a hydrogel matrix by systematically varying the nanoemulsion concentration through dilution with the continuous phase, and plotted the intensity as relative intensity ($I/I_{100\,\%}$), where $I_{100\,\%}$ denotes the signal of the undiluted nanoemulsion measured under identical acquisition settings (Figure 3g; Figure S9). Increasing the nanoemulsion content led to a linear increase in emission intensity, as expected for a concentration-dominated process in a homogeneous medium. This linear relationship contrasts sharply with the nonlinear, greater-than-sevenfold enhancement observed in dehydrated microdomes, demonstrating that structural optical confinement—specifically, multiple scattering and photon trapping within the high-index-contrast architecture—is the dominant mechanism. The quantitative relationship between this scattering microenvironment and upconversion amplification is further examined through speckle-resolved analysis in the following section.

2.4 | Reconfigurable Speckle-Engineering Enables Dynamic Modulation of Nonlinear Upconversion Luminescence

To experimentally verify the dynamic scattering tunability of the nanoemulsion-confined microdomes, we quantified the speckle characteristics of the 980 nm excitation field in both hydration states. Speckle contrast C, defined as the ratio of the standard deviation to the mean intensity ($C = \sigma/\langle I\rangle$), provides a direct measure of scattering-induced intensity fluctuations. The contracted (dehydrated) microdomes exhibit consistently higher speckle contrast (~0.35–0.45) than expanded (hydrated) microdomes (~0.17–0.25) across all relevant thicknesses (~50 μm for contracted, ~70 μm for expanded states), representing approximately a two-fold enhancement (Figure S10a). Furthermore, the average speckle grain size decreases from ~1.6 μm in the expanded state to ~1.4 μm in the contracted state, indicating the formation of finer, more localized excitation hot spots upon dehydration (Figure S10b). This enhanced speckle contrast and reduced grain size confirm that dehydration activates a strongly scattering microenvironment with pronounced intensity fluctuations. Given the nonlinear, multiphoton nature of the upconversion process, this speckle-engineered excitation field—where localized high-intensity hot spots drive disproportionately stronger emission—contributes significantly to the observed sevenfold luminescence enhancement.

To further understand this relationship, we performed numerical simulations to directly visualize the photoluminescence generated in the 3D volume of each microdome in the contracted and expanded states. To perform the simulations, we first measured the scattering mean free paths of both states. Since ballistic photons decay exponentially upon propagation through scattering media, we prepared samples of varying thicknesses for both states and measured the remaining ballistic photons after propagation through each sample. The scattering mean free paths for the contracted and expanded states were found to be 15.6 and 57.3 μm, respectively, demonstrating the dynamic and reconfigurable scattering engineering enabled by hydration and dehydration cycles (Figure S11).

Next, the anisotropy factor g, which describes the degree of direction change upon each scattering event, was quantified based on Mie scattering using the average size of the nanoemulsion droplets and the refractive indices of the droplets and the surrounding media [54]. The anisotropy factors g for the contracted and expanded states were found to be 0.5681 and 0.5385, respectively. The obtained scattering mean free path and anisotropy factor of each microdome state were used to design thin random phase plates displaying the corresponding scattering characteristics. The angular spectrum method was then used to propagate the optical field through all phase plates, enabling us to visualize the evolution of the excitation beam intensity profile along the microdome volume (Figure 4a,b) [55, 56]. As anticipated, the contracted state showed a faster development of speckles, resulting in excitation flux concentrating into multiple high-intensity hot spots (speckles) and brighter upconversion photoluminescence. This behavior originates from the nonlinear dependence of UCN upconversion on excitation intensity. Briefly, for the same total incident excitation energy, a speckle-like (interference-structured) excitation field—containing stochastic hot spots—drives nonlinear upconversion more efficiently than a spatially homogeneous excitation intensity distribution.

Finally, to quantitatively compare the overall photoluminescence brightness of each microdome under different speckle conditions, we integrated the depth-dependent emission predicted for each optical configuration. Importantly, the intrinsic nonlinearity of our UCN system was experimentally determined by excitation-flux-dependent measurements, which yield a log-log slope of 1.68 (Figure S12). Using this experimentally determined scaling, we incorporated the nonlinear upconversion response into the brightness calculation while assuming a uniform spatial distribution of UCN-loaded nanoemulsion droplets within the microdome. This treatment captures the key physical consequence of speckle formation—namely, that localized high-fluence hot spots contribute disproportionately to the net upconversion output—allowing a direct, configuration-by-configuration comparison of predicted microdome brightness under structured excitation fields. Considering the dilution of the UCN emulsion density, as well as the volume change upon expansion (hydration), we confirmed that a ~2.2-fold photoluminescence enhancement can be obtained based solely on the different speckle illumination characteristics between the two states (Figure 4c).

2.5 | Scattering-Enabled Photon Trapping and Geometry-Dependent Outcoupling Provide Cooperative Gain Beyond Speckle

While the scattered speckle illumination due to the heterogeneous refractive index distribution in the microdome design indeed enhanced the photoluminescence, it could not solely

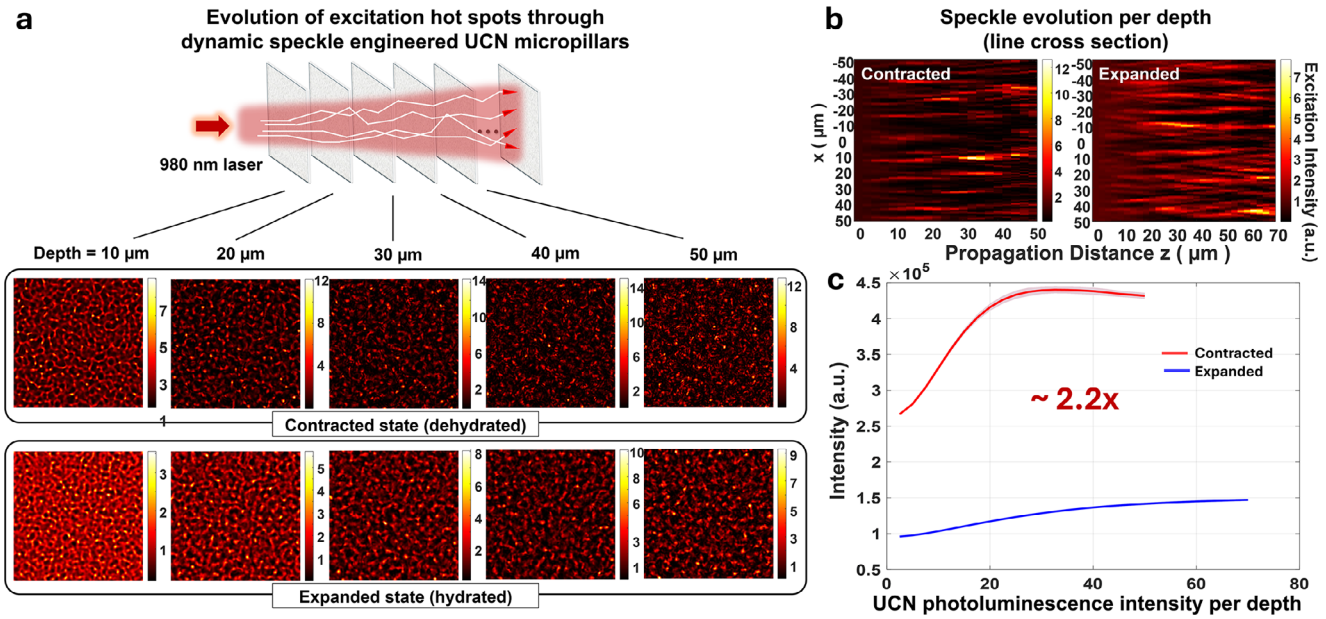

FIGURE 4 | Dynamic speckle engineering to exploit UCN nonlinear photoluminescence for reconfigurable soft upconversion photonics. (a) Wave propagation simulation visualizing the illumination intensity per depth inside UCN-loaded nanoemulsion microdomes. Top: schematic of the random phase plates model. Bottom: speckle illumination intensity distribution per depth for expanded and contracted states. (b) Line cross-sections of excitation intensity across microdome thickness. (c) Calculated UCN photoluminescence intensity per depth, showing ~2.2-fold enhancement between hydration and dehydration states. Dark lines: average photoluminescence obtained for over 100 random realizations of each scattering microdome, and the light shades show the standard deviation. Please note that the microdome in the expanded state is taller than in the contracted state, as shown in the graph.

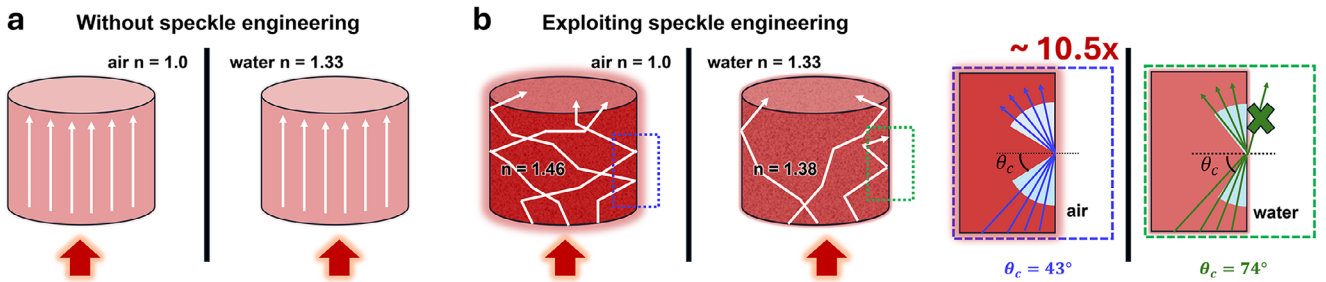

FIGURE 5 | Scattering-enabled waveguiding increases the pump photon residence time in contracted microdomes. (a) Without nanoemulsion-induced scattering, the 980 nm pump primarily propagates in a near-single pass, giving minimal path-length enhancement regardless of boundary condition (dry or wet). (b) With embedded UCN-loaded nanoemulsions, multiple scattering redistributes the excitation beam into a broad angular spectrum, enabling total internal reflection and extended optical paths. The microdome/air interface (contracted state, blue dotted square) supports a smaller critical angle than the microdome/water interface (expanded state, green dotted square), leading to stronger confinement and longer effective path length in the dry state.

explain the higher enhancement exceeding sevenfold that we observed in experiments. This higher enhancement is due to an additional advantage gained by extended optical path lengths (photon dwell time) through the microdome due to scattering and waveguiding effects associated with the high refractive index inhomogeneities in the composite structure (Figure 5). As in optical fibers, light propagating in a medium with a higher refractive index than the surrounding can undergo total internal reflection at the boundaries resulting in waveguiding of light. The effective *NA* (numerical aperture) of such a waveguide is given by $NA = \sqrt{n_{in}^2 - n_{out}^2}$, where n_{in} is the refractive index of the medium that light propagates in, and n_{out} is the refractive index of the surrounding medium. Light rays with angles within this effective *NA* will be guided through the waveguide via total internal reflection.

However, without speckle engineering, this does not result in reprogrammable change in photoluminescence as shown in Figure 5a. When there is no scattering to generate various angles of excitation light, the excitation beam simply passes through the entire structure in a single pass, regardless of the refractive index difference at the boundary. The UCNs within such a structure, therefore, only have the probability of being excited once during a single straight photon passage, whether the structure is dry or wet. However, when UCN-loaded nanoemulsions are embedded, the excitation light is scattered inside the microdome

waveguide, generating multiple paths with different respective angles (Figure 5b). For the contracted state (dehydrated), the refractive index difference between the microdome and air gives a critical angle of 43°, where all beams with higher angles are guided back into the microdome. Due to the scattering and multiple reflections, the effective optical path length is extended inside the microdome, resulting in a higher probability for the UCNs to be excited during the longer excitation beam path, even under the same incident illumination power. The expanded state (hydrated) also supports total internal reflection; however, for a higher angle of 74°, resulting in less scattered light that can be guided back into the microdomes. To be quantitative, we performed a Monte Carlo-type simulation where 2 million beams with random angles were generated and inserted into the corresponding waveguides. We made a simulation approximating micropillars with flat surface boundaries and compared the relative optical path lengths for the beams injected into the wet and dry micropillars. For incident beams encompassing an *NA* of 1, we found that the dry micropillars supported effective optical path lengths that are longer than the wet micropillars on average by 10.5-fold. Combining the previous enhancement from the speckle illumination alone, we now obtain a 23-fold overall dynamic photoluminescence enhancement between the two states based on first-order approximations. Considering that our first order approximations neglected light leakage due to surface irregularities, the exact microdome 3D shape geometry, and back reflection from multiple scattering, which result in overestimations, our simulations clearly demonstrate how speckle generation and waveguiding play a synergistic role in enabling the reconfigurable soft nonlinear photonic platform that we have demonstrated.

While simulations clearly demonstrate the synergy between structural optical confinement and nonlinear amplification of the speckle-engineered excitation field, we conducted further experiments to quantify the individual contributions of these synergistic effects. To decouple the role of structural optical confinement from that of nonlinear amplification, we leveraged the well-known saturation behavior of lanthanide-doped UCN photoluminescence nonlinearity at elevated excitation intensities. Under the practical excitation flux used throughout this work (~0.01 mW/μm^2), the UCN photoluminescence exhibits a nonlinearity exponent of 1.68 with respect to excitation intensity. As excitation flux is increased toward the saturation regime, this exponent decreases progressively toward 1.18 (near-linear, Figure S12). Crucially, the structural optical confinement effects — the refractive index landscape of the contracted microdome and the resulting scattering mean free path, and internal reflection-based waveguiding characteristics — are all independent of excitation intensity. Measuring the photoluminescence enhancement ratio between the contracted and expanded states as a function of excitation flux, therefore, provides a direct experimental window to isolate these two contributions. As shown in Figure S13, the enhancement ratio decreases progressively from ~7-fold at the practical excitation flux to ~3-fold as photoluminescence nonlinearity approaches saturation. This residual ~3-fold enhancement under near-linear excitation conditions represents the contribution of structural optical confinement alone — the combination of shortened scattering mean free path (15.6 μm in the contracted state vs. 57.3 μm in the expanded state) and enhanced internal reflection-based waveguiding arising from the larger refractive index contrast at the microdome/air interface (critical angle 43°) in the contracted state relative to the microdome/water interface (critical angle 74°) in the expanded state. The remaining ~2.3-fold factor is attributed to the nonlinear amplification of the speckle-engineered excitation field: in the contracted state, the higher speckle contrast (~0.35–0.45 vs. ~0.17–0.25 in the expanded state) generates localized high-intensity hot spots that drive disproportionately stronger upconversion emission through the multiphoton nature of the process. The ~2.3-fold contribution from speckle illumination combined with UCN nonlinearity is in close quantitative agreement with the simulated ~2.2-fold nonlinear enhancement (Figure 4c), providing independent validation of the physical model.

Taken together, the volumetric controls, speckle-resolved measurements, simulations, and photoluminescence saturation experiments provide a quantitative picture of the total ~7-fold enhancement in the contracted microdomes. Structural optical confinement — multiple scattering within the high-refractive-index-contrast nanoemulsion architecture and enhanced internal reflection-based waveguiding at the microdome/air interface — accounts for approximately 3-fold, while nonlinear amplification of the speckle-engineered excitation field by the multiphoton upconversion process contributes an additional approximately 2.3-fold. Acting synergistically, these two mechanisms together produce the observed greater-than-sevenfold brightness enhancement, well beyond what is achievable through emitter densification or structural confinement alone. While the 980 nm intensity exhibits strong speckle-like fluctuations on the micrometer scale, the corresponding green upconversion emission profile is considerably smoother and lacks a speckle signature. This behavior reflects the incoherent nature of the emission and indicates that the visible output effectively integrates over the structured excitation field, rather than reproducing its granular pattern.

2.6 | Structural and Optical Stability of Microdomes Containing Nanoemulsion Droplets

Large-area arrays of UCN-loaded nanoemulsion microdomes were fabricated using programmable DMD-based microlithography. The automated program enables rapid patterning based on user-defined parameters such as array dimensions, pitch, exposure dose, and dwell time (Movie S3). A representative 6 × 5 array of microdomes exhibits a high degree of structural and optical uniformity, with each dome measuring 200 μm in diameter at a center-to-center pitch of 400 μm (Figure 6a). The upconversion emission is highly homogeneous across the array. Line profile analysis of the luminescence confirms uniform peak intensities and spacing between adjacent domes (Figure 6b). Upon immersion in water, the array undergoes reversible intensity switching, with bright emission in the contracted (dehydrated) state and strongly attenuated emission in the expanded (hydrated) state. Time-resolved luminescence traces (integration time: 8 ms) show that the emission begins to decrease within ~25 ms after water contact, indicating a sub-0.1 s onset of the hydration-triggered ON-OFF response (Figure S14). Time-stamped frames from Figure S15 and Movie S2 further illustrate the practical switching dynamics, where the emission becomes

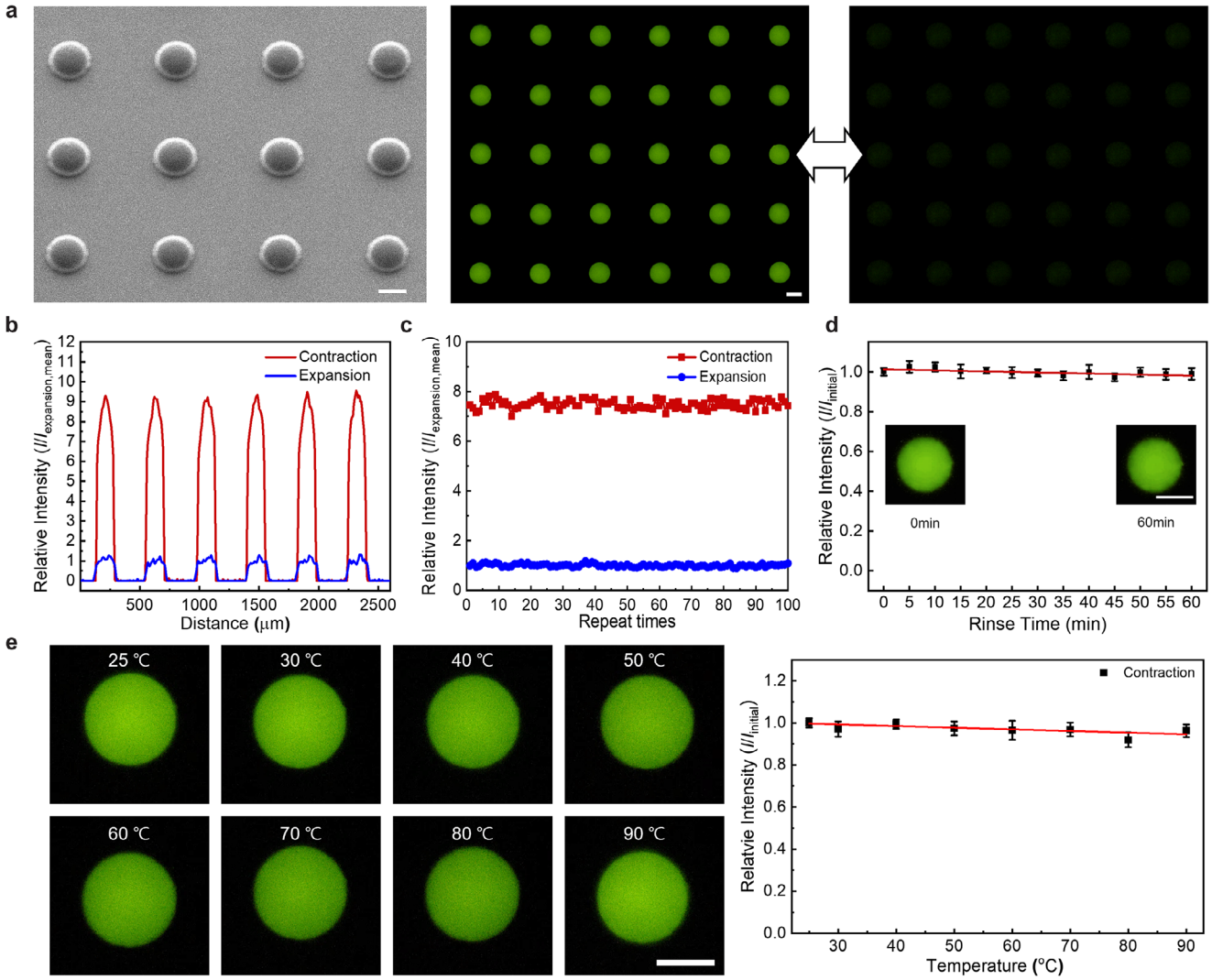

FIGURE 6 | Reversible optical switching and structural stability of nanoemulsion-confined microdomes. (a) SEM image of a representative 4 × 3 sub-region of a 6 × 5 microdome array (shown to resolve individual dome morphology), together with luminescence images of the 6 × 5 array in the contracted and expanded states. Scale bar: 100 μm. (b) Line profiles are shown as relative intensity ($I/I_{Expansion,mean}$), normalized to the mean intensity of the dehydrated (contracted) state measured along the same line. (c) Cycling stability of luminescence switching over 100 hydration–dehydration cycles. Relative intensity ($I/I_{Expansion,mean}$) is normalized to the mean intensity of the expansion state. (d) Long-term rinsing stability over 60 min, showing negligible loss in emission intensity. Relative intensity ($I/I_{Initial}$) is normalized to the initial intensity. (insets: luminescence images at 0 and 60 min). Scale bar: 100 μm. (e) Thermal stability from 25 to 90°C (left) and Relative intensity plot ($I/I_{Initial}$) (right). Scale bar: 100 μm.

strongly attenuated within seconds under direct water exposure. This ON–OFF switching behavior persists over at least 100 hydration–dehydration cycles with <4 % ON-state drift, demonstrating excellent mechanical and optical durability (Figure 6c; Figure S16 and Note S3). For cycling tests, hydration was induced by placing a water droplet on the glass substrate to fully swell the microdomes, and dehydration was achieved by N_2-gun blowing for 30 s; because residual moisture can continue to evaporate under NIR illumination and cause a gradual intensity drift, the "ON" state was recorded only after the emission reached a stable plateau.

We next evaluated the chemical stability of the encapsulated droplets within the hydrogel matrix. Continuous rinsing of the microdome array in water for up to 60 min produced no significant change in emission intensity (Figure 6d; Figure S17), indicating strong retention of UCN-loaded FC-40 droplets with minimal leaching or coalescence. The thermal stability of the microdomes was further assessed on a temperature-controlled stage by monitoring the luminescence at 10°C increments from 25°C to 90°C (Figure 6e; Figure S18). Over this range, both microdome geometry and upconversion intensity remained essentially constant, with only minor variation observed at the highest temperatures. This indicates that the crosslinked PEGDA network effectively stabilizes the nanoemulsion droplets against thermal destabilization—a common limitation of conventional nanoemulsion systems. Together, these results demonstrate that the nanoemulsion-confined PEGDA microdome architecture provides robust, reversible, and spatially uniform optical switching while maintaining colloidal and structural integrity under repeated cycling, prolonged aqueous exposure, and elevated temperatures.

2.7 | Programmable and Environment-Responsive Photonic Encoding with Microdome Architectures

To demonstrate the programmable and environment-responsive optical functionality of the nanoemulsion-confined microdome system, we fabricated a series of pattern-encoded photonic arrays with spatially defined luminescence. These examples highlight the utility of the hydrogel architecture for information display, concealment, and environment-sensitive encoding. As illustrated in Figure 7a, pre-patterned letters composed of multicolor UCNs (green, blue, yellow, white, and red; Table S3) embedded in a rigid polyurethane acrylate (PUA) matrix were overlaid with nanoemulsion microdomes (Figures S19 and S20 and Tables S4 and S5). Owing to their reversible swelling and contraction behavior, the microdomes optically conceal or reveal the underlying letters depending on the hydration state. In the dry state, bright and uniform upconversion emission from the microdome layer masks the background, whereas in the swollen state, the microdome emission is strongly quenched, and the embedded multicolor "HELLO" pattern in the PUA layer—unaffected by hydration—appears clearly in both luminescence and bright-field images (Figure 7a). This dual-modality readout enables controlled visibility switching, offering potential applications in dynamic labeling or anti-counterfeiting.

Beyond concealment, the high-resolution capability of our customized DMD-based microlithography system enables patterning of individual microdomes into custom shapes with sharp emission boundaries, ranging from simple polygons to more intricate icons (Figure 7b). These geometrically defined structures demonstrate the versatility of the microdome lithography platform for generating complex photonic layouts. The scalability of the process is further demonstrated in Figure 7c, where a large-area array of green nanoemulsion microdomes conceals underlying UCNs patterns in a PUA matrix depicting emoji faces with distinct colors (red, green, and white). In the contracted state, the bright microdome emission obscures the background. Local swelling upon underwater immersion selectively quenches emission in targeted regions, allowing the hidden faces to emerge with high spatial fidelity and on/off contrast.

The system also offers programmable thresholds for information reveal. A key advantage is that the relative brightness of the background layer can be tuned by adjusting the UCNs concentration in the PUA matrix, thereby setting the environmental threshold at which hidden information becomes visible. In one demonstration, a 3 × 3 Rubik's cube motif composed of blue, green, and red UCNs domains is overlaid with nanoemulsion microdomes. In the dry state, all tiles exhibit bright, uniform emission; upon hydration, selective quenching of the nanoemulsion-covered tiles produces a new color pattern, effectively re-encoding the displayed information. Although minor intensity variations between tiles are visible due to imperfect concentration matching between the nanoemulsion and PUA layers, the reversible pattern transformation is clearly demonstrated. With further optimization of the UCN concentration matching between layers, the number and spatial arrangement of nanoemulsion-covered tiles can be precisely programmed to encode a large combinatorial information space within a single microdome array. (Figure 7d). In a simpler configuration, a microdome array integrated on a substrate functions as a moisture-responsive tag whose luminescence can be toggled between bright and dim states, enabling transient labeling under NIR excitation (Figure 7e). These examples illustrate how the hydration-dependent optical switching of nanoemulsion microdomes can be leveraged to create stimuli-responsive information systems with tunable reveal thresholds.

As a final demonstration, we realized a spatially encoded photonic QR code composed of bright nanoemulsion microdomes and dimmer PUA domains. In the dehydrated state, the intensity contrast between the two components yields a clearly readable QR pattern under 980 nm excitation (Movies S4 and S5). Upon hydration, the nanoemulsion emission is selectively quenched, and the code becomes invisible, while remaining undetectable under standard bright-field illumination (Figure 7f; Figure S21). Because different UCNs' colors can be readily achieved by varying the dopant composition, each color channel can serve as an independent encoding dimension. This underscores the potential of the platform for multilevel, stimuli-responsive photonic security applications.

3 | Conclusion

We have established a nanoemulsion-confined microdome platform that couples structural reconfigurability with strong, filter-free amplification of upconversion luminescence. UCN-loaded fluorocarbon nanoemulsion droplets are immobilized within a photo-crosslinked PEGDA hydrogel matrix and digitally patterned via DMD-based maskless lithography into microdomes. Distinct from conventional approaches relying on rigid substrates or complex nanoparticle surface treatments, this soft photonic architecture delivers robust optical performance without such constraints. Hydration–dehydration cycles reversibly switch the microdomes between weakly and highly emissive states, yielding greater than sevenfold brightness change. Speckle-resolved optical analysis reveals that the contracted microdomes exhibit consistently higher speckle contrast (~0.35–0.45) than expanded microdomes (0.17–0.25) across all measured thicknesses, confirming enhanced scattering-induced intensity fluctuations in the dehydrated state. This difference correlates with the observed luminescence amplification, consistent with the nonlinear, multiphoton nature of upconversion. The speckle-engineered microenvironment generates localized excitation hot spots, extends the photon path length via internal reflection, while the invisible NIR pump enables filter-free readout. The platform maintains stability over 100+ switching cycles and elevated temperatures. We demonstrated moisture-responsive message concealment, multicolor patterning, and reversible QR-code encryption for optical security applications. This work introduces a general strategy integrating nanoemulsion templating, refractive-index engineering, and soft lithographic patterning, with potential extension toward wearable sensors and adaptive displays.

4 | Experimental Section

4.1 | Materials

Poly(ethylene glycol) diacrylate (PEGDA, MW 700 g/mol), 2-hydroxy-2-methylpropiophenone (Darocur 1173), oleic acid, gadolinium chloride hexahydrate ($GdCl_3 \cdot 6H_2O$), ytterbium

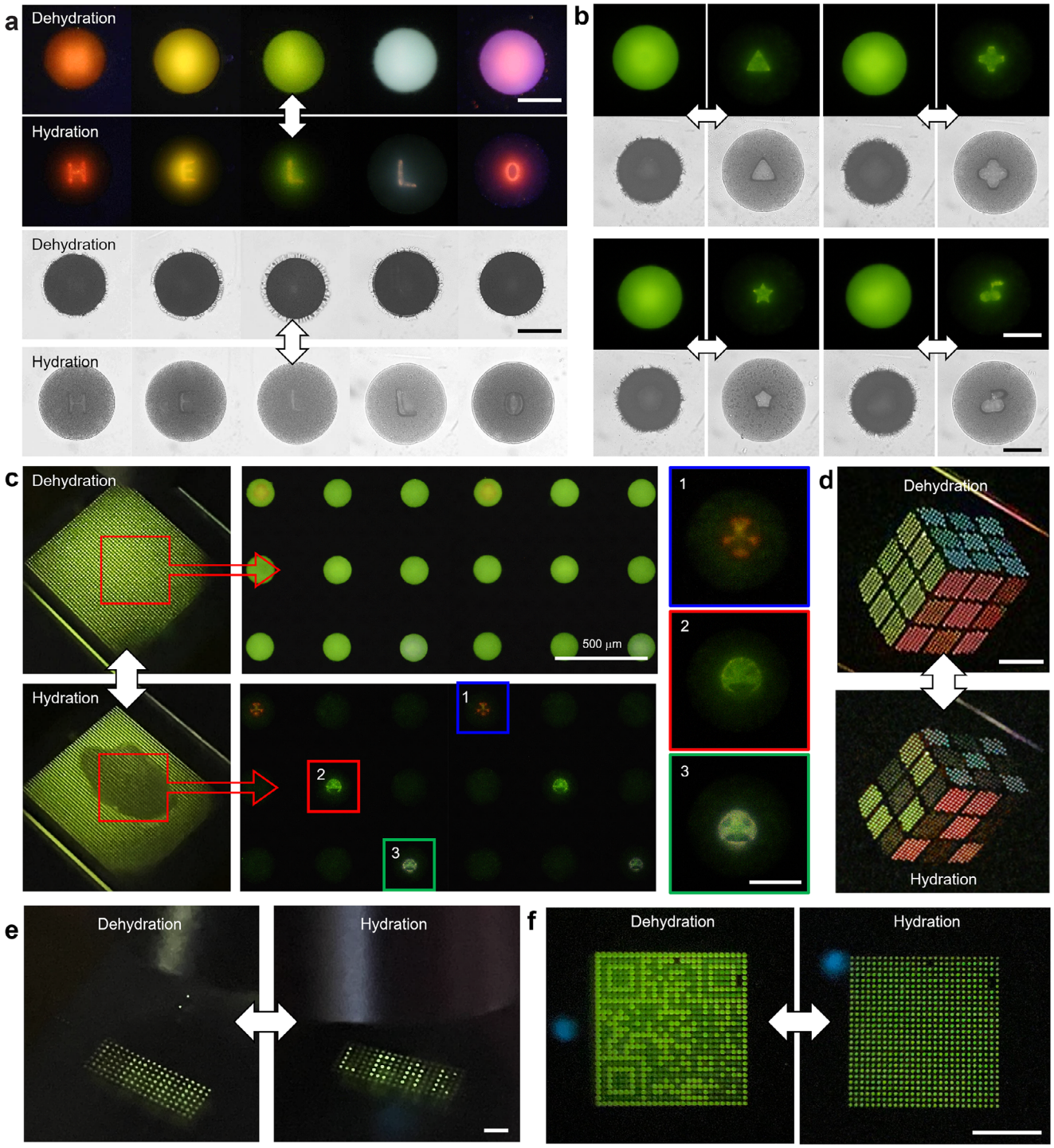

FIGURE 7 | Programmable, reversible, and moisture-responsive photonic encoding using nanoemulsion-confined microdomes. (a) Multicolor "HELLO" pattern with reversible luminescence concealment. Scale bar: 100 μm. (b) Custom-shaped microdomes fabricated by DMD microlithography. Scale bar: 100 μm. (c) Large-area microdome array concealing multicolored emoji patterns. Insets 1–3: magnified views. (red: angry, green: smiley, white: confused). Scale bars: 500 μm (middle), 100 μm (right). (d) Rubik's cube-inspired multicolor motif with hydration-induced pattern change. Scale bar: 0.5 cm. (e) Macroscopic moisture-responsive tag. Scale bar: 1 mm. (f) Photonic QR code with reversible information encryption. Scale bar: 0.5 cm.

chloride hexahydrate ($YbCl_3 \cdot 6H_2O$), yttrium chloride hexahydrate ($YCl_3 \cdot 6H_2O$), erbium chloride hexahydrate ($ErCl_3 \cdot 6H_2O$), thulium chloride hexahydrate ($TmCl_3 \cdot 6H_2O$), and ammonium fluoride (NH_4F) were purchased from Sigma–Aldrich. Polyurethane acrylate (PUA) was obtained from Changsung. FC-40 was purchased from Alachua, and Pluronic F-68 (PF-68) was obtained from Gibco (Life Technologies). Phosphotungstic acid, ethanol, and sodium hydroxide were purchased from Daejung Chemicals. All chemicals were used as received without further purification.

4.2 | Synthesis of Rod-Shaped β-$NaREF_4$ (RE = Gd, Y, Yb, Er, and Tm) UCNs

In a 50 mL Teflon liner autoclave vessel, 3 mL of NaOH solution was added, followed by the dropwise addition of 10 mL ethanol and 10 mL oleic acid under vigorous stirring. Subsequently, 2 mL of rare-earth chloride solution (0.2 M $RECl_3 \cdot 6H_2O$, RE = Y, Yb, Er, Tm, Gd) was added dropwise. Then, 4 mL of 2 M NH_4F was introduced, and the mixture was stirred vigorously for 10 min. The Teflon liner was sealed in an autoclave and heated at 200°C for 3 h. The resulting nanoparticles were collected and washed five times with ethanol and deionized water (DIW) by centrifugation (5000 rpm, 5 min). The rare-earth dopant composition of the UCNs was controlled by the molar feed ratios of $RECl_3$ precursors. The dopant compositions used for multicolor demonstrations (blue/green/red) are summarized in Table S3, and the corresponding emission spectra are provided in Figure S19.

4.3 | Fabrication of UCN-Loaded Nanoemulsion Precursor Solution

The nanoemulsion precursor was prepared by forming a UCN-dispersed FC-40 oil phase and a PEGDA-based aqueous phase, followed by pre-emulsification and high-pressure homogenization. For the oil phase, 1.0 g of hydrophobic green UCNs (β-$NaYF_4$-based; dopant composition specified in Table S3) was added to 50 mL of FC-40 and magnetically stirred for ≥2 h to obtain a uniform dispersion. For the aqueous phase, 36 mL of PEGDA (Mn 700) and 59 mL of DI water were mixed in a 300 mL beaker under magnetic stirring for ≥20 min. Then, 5 mL of Pluronic F-68 solution (40 mM) was added, and the mixture was stirred for ≥10 min. The oil phase was then added slowly (dropwise) into the aqueous phase under vigorous stirring and further stirred for ≥30 min to form a coarse pre-emulsion. To improve dispersion prior to homogenization, the pre-emulsion was subjected to vortex mixing (5 min) followed by cup-horn sonication (10 min). The pre-emulsion was subsequently processed using a high-pressure homogenizer (Panda Plus 2000, GEA Niro Soavi) at 15 000 psi for 15 passes to obtain a stable oil-in-water nanoemulsion. After homogenization, the nanoemulsion was stored at ≤4°C for 24 h to stabilize the droplet population prior to microgel fabrication.

4.4 | Fabrication of UCNs Nanoemulsion-Confined Microdome Arrays

A 130 μm-thick polyimide tape was placed on an acrylated glass slide and covered with a PDMS-coated glass plate. A solution containing 100 μL of the nanoemulsion and 2 μL of Darocur 1173 was injected into the gap defined by the spacer. A hydrogel microdome was fabricated using a DMD-based UV lithography system (UV intensity: 3.09 mW/cm^2). After exposure, the unpolymerized precursor solution was removed by rinsing with water.

4.5 | Fabrication of UCN Nanoemulsion-Confined Microdomes With Hidden Patterns and Letters

Microdome structures encoding hidden letters and patterns were fabricated using a customized DMD-patterned microlithography setup. 4 mg of UCNs were uniformly dispersed in 90 μL of PUA using ultrasonication. For the inner-letter precursor, 90 μL of UCNs dispersed PUA solution was mixed with 10 μL of Darocur 1173. The solution was injected between two glass substrates separated by a 35 um polyimide spacer and exposed to DMD-patterned 365 nm UV light (0.927 mW/cm^2). After polymerization, the uncured precursor solution was rinsed with ethanol. For the overlaid microdomes, a 130 μm imide spacer was placed on an acrylated glass slide and covered with a PDMS-coated glass plate. A solution containing 100 μL of nanoemulsion and 2 μL of Darocur 1173 was injected into the spacer-defined channel. Hydrogel microdomes were then formed by DMD-patterned 365 nm UV light (3.09 mW/cm^2), and unpolymerized precursor solution was removed by rinsing with water (Note S4 and Table S4).

4.6 | Imaging and Spectral Analysis of UCN-Loaded Nanoemulsion and Microdomes

The luminescence of the UCNs-loaded nanoemulsion and microdomes was measured using a 500 mW 980 nm NIR laser with a customized optical setup having a circular irradiation area (Diameter: 220 μm) (MDL-F-980-5W, Changchun New Industries Optoelectronics Tech. Co., Ltd.). A Nikon D-810 camera with a ×20 objective was used for color imaging, and upconversion luminescence spectra were recorded using a Nikon Ti-E inverted microscope installed with the photoluminescence spectrometer (QEPRO-FL, Ocean Optics).

4.7 | Side-View Imaging and Volume Estimation of Microdomes

The side view of fabricated microdomes was obtained using the CCD camera of a microscope system. The microdomes were exposed under various swelling conditions determined by the mixing ratio of PEG200 and water, including the dehydrated state. Based on these images, the cross-sectional profiles of individual posts were plotted using the Desmos software. The resulting curves were then revolved around the *y*-axis using the Wolfram Alpha platform to calculate the corresponding volumes, taking into account the image scale applied.

4.8 | Characterization

UCNs are characterized by scanning electron microscope (S-4800, Hitachi) and transmission electron microscopy (JEM-2100, JEOL). For TEM analysis, the sample was diluted to 10 % in deionized water and deposited onto a formvar-coated copper grid for 3 min. After sufficient penetration, the specimen was stained with 2 % phosphotungstic acid for 2 min and subsequently cured under UV light. Upconversion luminescence spectra were

recorded using a high-sensitivity spectrometer (QE Pro-FL, Ocean Optics). Droplet size distribution of nanoemulsion was measured by dynamic light scattering (Nano ZS, Malvern). The transmittance of UCN-loaded PEG nanoemulsion solutions and nanoemulsion-confined microdomes was measured using a UV–vis microspectrometer (20/20/PV, CRAIC). Optical images were captured using a DSLR camera (D810, Nikon) and a smartphone camera (iPhone 12 mini, Apple).

Acknowledgements

This study was supported by the National Research Foundation of Korea (NRF) grant funded by the Korean government (MSIT) (RS-2022-NR070257).

Conflicts of Interest

No. The authors declare no conflict of interest.

Data Availability Statement

The data that support the findings of this study are available in the supplementary material of this article.

References

1. H. Liu, Y. Wang, Z. Shi, et al., "Fast Self-Assembly of Photonic Crystal Hydrogel for Wearable Strain and Temperature Sensor," *Small Methods* 6 (2022): 2200461.

2. L. Cai, Y. Wang, L. Sun, J. Guo, and Y. Zhao, "Bio-Inspired Multi-Responsive Structural Color Hydrogel with Constant Volume and Wide Viewing Angles," *Advanced Optical Materials* 9 (2021): 2100831.

3. J. Zhang, Q. Li, C. Dai, et al., "Hydrogel-Based, Dynamically Tunable Plasmonic Metasurfaces with Nanoscale Resolution," *Small* 18 (2022): 2205057.

4. B. Ko, J. Kim, Y. Yang, et al., "Humidity-Responsive RGB-Pixels via Swelling of 3D Nanoimprinted Polyvinyl Alcohol," *Advanced Science* 10 (2023): 2204469.

5. C. Dai, Z. Li, Z. Li, et al., "Direct-Printing Hydrogel-Based Platform for Humidity-Driven Dynamic Full-Color Printing and Holography," *Advanced Functional Materials* 33 (2023): 2212053.

6. T. Yu, B. Wang, and L. P. Yu, "Dual-Mode Color-Changing pH Sensor Based On Fluorescent MOF Embedded Photonic Crystal Hydrogel," *Journal of the Chinese Chemical Society* 69 (2022): 831–839.

7. H. L. Marks, K. Cook, E. Roussakis, et al., "Quantitative Luminescence Photography of a Swellable Hydrogel Dressing with a Traffic-Light Response to Oxygen," *Advanced Healthcare Materials* 11 (2022): 2101605.

8. S. S. Sanker, S. Thomas, S. Nalini, D. P. Jacob, V. S. Suniya, and K. N. Madhusoodanan, "Smartphone-Based Molecularly Imprinted Photonic Crystal Hydrogel Sensor For The Label-Free Detection Of Bisphenol A," *Macromolecular Chemistry and Physics* 225 (2024): 2400043.

9. H. Lv, W. Zheng, Y. Wang, Z. Hu, Y. Chen, and Y. Wang, "Opal Photonic Crystal Double-Network Hydrogel For Visual Detection Through Structural Color And Fluorescent Responsiveness," *Journal of Applied Polymer Science* 141 (2024): 55339.

10. S. Daqiqeh Rezaei, J. Ho, A. Naderi, et al., "Tunable, Cost-Effective, And Scalable Structural Colors For Sensing And Consumer Products," *Advanced Optical Materials* 7 (2019): 1900735.

11. J. Guo, J. Tuo, J. Sun, et al., "Stretchable Multimodal Photonic Sensor for Wearable Multiparameter Health Monitoring," *Advanced Materials* 37 (2025): 2412322.

12. M. Jiang, C. Han, Z. Cao, et al., "Microcrack-Structured Visualizable Hydrogel Sensor For Machine Learning-Assisted Handwriting Recognition," *Advanced Functional Materials* 36 (2025): 12316.

13. Y. Xia, S. Gao, R. Yu, et al., "Near-Infrared Light Induced Dynamic Structural Color Change of Amorphous Photonic Hydrogel," *ACS Applied Polymer Materials* 3 (2021): 757–764.

14. Z. Li, P. Liu, X. Ji, et al., "Bioinspired Simultaneous Changes in Fluorescence Color, Brightness, and Shape of Hydrogels Enabled by AIEgens," *Advanced Materials* 32 (2020): 1906493.

15. F. Fu, L. Shang, Z. Chen, Y. Yu, and Y. Zhao, "Bioinspired Living Structural Color Hydrogels," *Science Robotics* 3 (2018): aar8580.

16. J. Xue, M. Yao, G. Wang, et al., "An Environmental Perception Self-Adaptive Discolorable Hydrogel Film toward Sensing and Display," *Advanced Optical Materials* 9 (2021): 2100116.

17. Y. Sun, X. Le, H. Shang, et al., "Dual-Mode Hydrogels With Structural And Fluorescent Colors Toward Multistage Secure Information Encryption," *Advanced Materials* 36 (2024): 2401589.

18. Z. Lin, H. Wang, H. Xiang, et al., "Orthogonal Photo- and Thermo-Responsive Fluorescent Polymeric Hydrogels for Multi-Level Information Encryption and Anti-Counterfeiting," *Advanced Optical Materials* 12 (2024): 2401604.

19. H. Yang, S. Li, J. Zheng, et al., "Erasable, Rewritable, and Reprogrammable Dual Information Encryption Based on Photoluminescent Supramolecular Host–Guest Recognition and Hydrogel Shape Memory," *Advanced Materials* 35 (2023): 2301300.

20. Z. Hu, W. Tang, and X. Ji, "Application of Organic Gel on Skin Realized by Hydrogel/Organic Gel Adhesion," *Macromolecular Rapid Communications* 45 (2024): 2400371.

21. R. Xu, C. Qiao, M. Xia, et al., "Stable quantum dots/polymer matrix and their versatile 3D printing frameworks," *Journal of Materials Chemistry C* 9 (2021): 7194.

22. J. Du, W. Zhu, X. She, et al., "A Robust And Fluorescent Nanocomposite Hydrogel With An Interpenetrating Polymer Network Based On Graphene Quantum Dots," *Polymer Engineering & Science* 63 (2023): 2169–2179.

23. S. Shikha, X. Zheng, and Y. Zhang, "Upconversion Nanoparticles-Encoded Hydrogel Microbeads-Based Multiplexed Protein Detection," *Nano-Micro Letters* 10 (2018): 31.

24. M. Gao, J. Li, X. Lu, et al., "Lanthanides-Based Invisible Multicolor Luminescent Hydrogels And Films For Anti-Counterfeiting," *Inorganica Chimica Acta* 560 (2024): 121813.

25. F. Auzel, "Upconversion and anti-stokes processes with f and d ions in solids," *Chemical Reviews* 104 (2004): 139.

26. J. Lee, P. W. Bisso, R. L. Srinivas, J. J. Kim, A. J. Swiston, and P. S. Doyle, "Universal Process-Inert Encoding Architecture For Polymer Microparticles," *Nature Materials* 13 (2014): 524.

27. Y. Liu, S. Liang, C. Yuan, et al., "Fabrication of Anticounterfeiting Nanocomposites with Multiple Security Features via Integration of a Photoresponsive Polymer and Upconverting Nanoparticles," *Advanced Functional Materials* 31 (2021): 2103908.

28. C. Son, J. Kim, D. Kang, et al., "Behavioral Biometric Optical Tactile Sensor For Instantaneous Decoupling Of Dynamic Touch Signals In Real Time," *Nature Communications* 15 (2024): 8003.

29. J. Kim, S. Lee, Y. Jeong, et al., "Unlocking Multimodal Nonlinear Microscopy for Deep-Tissue Imaging under Continuous-Wave Excitation with Tunable Upconverting Nanoparticles," *Advanced Materials* 37 (2025): 2502739.

30. H. L. Wei, W. Zheng, X. Zhang, et al., "Tuning Near-Infrared-To-Ultraviolet Upconversion in Lanthanide-Doped Nanoparticles for Biomedical Applications," *Advanced Optical Materials* 11 (2023): 2201716.

31. M. S. Arai and A. S. de Camargo, "Exploring The Use Of Upconversion Nanoparticles In Chemical And Biological Sensors: From Surface

Modifications To Point-Of-Care Devices," *Nanoscale Advances* 3 (2021): 5135–5165.

32. M. Quintanilla, E. Hemmer, J. Marques-Hueso, et al., "Cubic Versus Hexagonal – Phase, Size And Morphology Effects On The Photoluminescence Quantum Yield of $NaGdF_4$:Er^{3+}/Yb^{3+} Upconverting Nanoparticles," *Nanoscale* 14 (2022): 1492–1504.

33. M. Haase and H. Schäfer, "Upconverting Nanoparticles," *Angewandte Chemie International Edition* 50 (2011): 5808–5829.

34. S. Liu, L. Yan, J. Huang, Q. Zhang, and B. Zhou, "Controlling Upconversion In Emerging Multilayer Core–Shell Nanostructures: From Fundamentals To Frontier Applications," *Chemical Society Reviews* 51 (2022): 1729–1765.

35. K. Huang, H. Liu, M. Kraft, et al., "A Protected Excitation-Energy Reservoir For Efficient Upconversion Luminescence," *Nanoscale* 10 (2018): 250–259.

36. D. Baek, T. K. Lee, I. Jeon, et al., "Multi-Color Luminescence Transition of Upconversion Nanocrystals via Crystal Phase Control with SiO_2 for High Temperature Thermal Labels," *Advanced Science* 7 (2020): 2000104.

37. D. Li, X. Liu, and J. Qiu, "Probing Interaction Distance of Surface Quenchers in Lanthanide-Doped Upconversion Core–Shell Nanoparticles," *The Journal of Physical Chemistry C* 122 (2018): 10278–10283.

38. C. L. Hofmann, S. Fischer, E. H. Eriksen, et al., "Experimental Validation Of A Modeling Framework For Upconversion Enhancement in 1D-Photonic Crystals," *Nature Communications* 12 (2021): 104.

39. Y. Shi, F. Zhang, J. Xu, et al., "Upconversion Fluorescence Enhancement of $NaYF_4$:Yb/Re Nanoparticles By Coupling With SiO_2 Opal Photonic Crystals," *Journal of Materials Science* 54 (2019): 8461–8471.

40. Y. Meng, D. Huang, H. Li, et al., "Bright Single-Nanocrystal Upconversion at Sub 0.5 W cm^{-2} Irradiance Via Coupling To Single Nanocavity Mode," *Nature Photonics* 17 (2023): 73–81.

41. J. Xu, Z. Dong, M. Asbahi, et al., "Multiphoton Upconversion Enhanced by Deep Subwavelength Near-Field Confinement," *Nano Letters* 21 (2021): 3044–3051.

42. L. Liang, D. B. Teh, N.-D. Dinh, et al., "Upconversion Amplification Through Dielectric Superlensing Modulation," *Nature Communications* 10 (2019): 1391.

43. Y.-T. Tseng, Y.-C. Chiu, V.-D. Pham, et al., "Ultrasensitive Upconversion Nanoparticle Immunoassay For Human Serum Cardiac Troponin I Detection Achieved With Resonant Waveguide Grating," *ACS Sensors* 9 (2024): 455.

44. B. Ko, N. Jeon, J. Kim, et al., "Hydrogels for Active Photonics," *Microsystems & Nanoengineering* 10 (2024): 1.

45. C. F. Guimarães, R. Ahmed, A. P. Marques, R. L. Reis, and U. Demirci, "Engineering Hydrogel-Based Biomedical Photonics: Design, Fabrication, and Applications," *Advanced Materials* 33 (2021): 2006582.

46. D. Ghindani, I. Issah, S. Chervinskii, et al., "Humidity-Controlled Tunable Emission in a Dye-Incorporated Metal–Hydrogel–Metal Cavity," *ACS Photonics* 9 (2022): 2287–2294.

47. J. Shin, P. V. Braun, and W. Lee, "Fast Response Photonic Crystal pH Sensor Based On Templated Photo-Polymerized Hydrogel Inverse Opal," *Sensors and Actuators B: Chemical* 150 (2010): 183–190.

48. J.-G. Park, W. Benjamin Rogers, S. Magkiriadou, et al., "Photonic-Crystal Hydrogels With A Rapidly Tunable Stop Band And High Reflectivity Across The Visible," *Optical Materials Express* 7 (2016): 253.

49. B. Yoo, C. Ryu, S. Lee, et al., "High-Throughput Multiplexed Plasmonic Color Encryption of Microgel Architectures via Programmable Dithering-Mask Flow Microlithography," *Advanced Materials* 37 (2025): 2405388.

50. J. Oh, D. Baek, T. K. Lee, et al., "Dynamic Multimodal Holograms Of Conjugated Organogels Via Dithering Mask Lithography," *Nature Materials* 20 (2021): 385–394.

51. Y. Shin, I. Jeon, Y. You, et al., "Facile Microfluidic Fabrication of 3D Hydrogel SERS Substrate with High Reusability and Reproducibility via Programmable Maskless Flow Microlithography," *Advanced Optical Materials* 8 (2020): 2001586.

52. S. Jacob, F. S. Kather, S. H. Boddu, J. Shah, and A. B. Nair, "Innovations in Nanoemulsion Technology: Enhancing Drug Delivery for Oral, Parenteral, and Ophthalmic Applications," *Pharmaceutics* 16 (2024): 1333.

53. Y. Singh, J. G. Meher, K. Raval, et al., "Nanoemulsion: Concepts, Development And Applications In Drug Delivery," *Journal of Controlled Release* 252 (2017): 28.

54. W. J. Wiscombe, "Improved Mie scattering algorithms," *Applied Optics* 19 (1980): 1505.

55. J. Yang, J. Li, S. He, and L. V. Wang, "Angular-Spectrum Modeling Of Focusing Light Inside Scattering Media By Optical Phase Conjugation," *Optica* 6 (2019): 250.

56. X. Cheng, Y. Li, J. Mertz, et al., "Development Of A Beam Propagation Method To Simulate The Point Spread Function Degradation In Scattering Media," *Optics Letters* 44 (2019): 4989.

Supporting Information

Additional supporting information can be found online in the Supporting Information section.

Supporting File: adfm75523-sup-0001-SuppMat.docx

Supplemental File: adfm75523-sup-0002-MovieS1.mp4.

Supplemental File: adfm75523-sup-0003-MovieS2.mp4.

Supplemental File: adfm75523-sup-0004-MovieS3.mp4.

Supplemental File: adfm75523-sup-0005-MovieS4.mp4.

Supplemental File: adfm75523-sup-0006-MovieS5.mp4.